Original Article

Subchondral Implantation of Artemisinin-Loaded Hyaluronic Acid Methacrylate Hydrogel Ameliorates Osteoarthritis

Jianxiang Teng[1,2,3,†], Daizhu Yuan[1,†], Chengming Wen[4], Sheng Zhou[2], Mengli Xie[1], Lian Zhu[1], Jiazhao Pan[1], Tianqi Zhou[1], Chuan Ye[1], Wei Seong Toh[4], Long Yang[1,5,*] and Xiaobin Tian[1,2,*]

[1]Department of Orthopedics, The Affiliated Hospital of Guizhou Medical University, 550004 Guiyang, Guizhou, China
[2]School of Basic Medical Sciences, Guizhou Medical University, 561113 Guiyang, Guizhou, China
[3]Department of Orthopedics and Joints, Chongqing Qianjiang Central Hospital, 409000 Chongqing, China
[4]Department of Orthopaedic Surgery, Yong Loo Lin School of Medicine, National University of Singapore, 119228 Singapore, Singapore
[5]Department of Orthopedics, Liupanshui Municipal People's Hospital, 553000 Liupanshui, Guizhou, China
[†]These authors contributed equally.

Abstract

Background: Knee osteoarthritis (KOA) involves pathological subchondral bone remodeling and aberrant bone–cartilage crosstalk. This study investigated Runt-related transcription factor 2 (*Runx2*) upregulation in osteoarthritis (OA) osteoblasts and evaluated an artemisinin-loaded hyaluronic acid methacryloyl (HAMA-ART) hydrogel for localized modulation of the subchondral bone microenvironment. **Methods:** HAMA-ART was characterized for morphology, chemical composition, ART release, degradation, mechanical properties, and biocompatibility. Its effects on osteoblast–chondrocyte paracrine communication were assessed *in vitro* using conditioned medium-based experiments. Therapeutic efficacy was evaluated by *in situ* implantation into the subchondral bone of a rat OA model induced by destabilization of the medial meniscus. **Results:** HAMA-ART exhibited a porous network, sustained ART release, gradual degradation, and acceptable biocompatibility. It attenuated aberrant *Runx2* upregulation in OA osteoblasts and reduced their pathological paracrine effects on chondrocytes, as indicated by decreased Matrix Metalloproteinase 13 (*MMP13*) and Type X Collagen (*COLX*) expression and preserved Type II Collagen Alpha 1 (*COL2A1*) expression. *In vivo*, HAMA-ART ameliorated OA-associated subchondral bone microstructural deterioration. Histological analysis showed lower Mankin scores, preserved cartilage thickness, and improved cartilage matrix homeostasis compared with untreated OA controls. **Conclusions:** HAMA-ART attenuated *Runx2* upregulation in OA osteoblasts and alleviated subchondral bone remodeling and cartilage degeneration. Localized subchondral delivery may provide a potential strategy for OA treatment.

Keywords: Osteoarthritis, subchondral bone, artemisinin, bone–cartilage crosstalk, hydrogel.

***Address for correspondence**: Long Yang, Department of Orthopedics, The Affiliated Hospital of Guizhou Medical University, 550004 Guiyang, Guizhou, China; Department of Orthopedics, Liupanshui Municipal People's Hospital, 553000 Liupanshui, Guizhou, China. E-mail: longyangchina@hotmail.com; Xiaobin Tian, Department of Orthopedics, The Affiliated Hospital of Guizhou Medical University, 550004 Guiyang, Guizhou, China; School of Basic Medical Sciences, Guizhou Medical University, 561113 Guiyang, Guizhou, China. E-mail: txb6@vip.163.com.

Copyright policy: © 2026 The Author(s). Published by Forum Multimedia Publishing, LLC. This article is distributed in accordance with Creative Commons Attribution Licence (http://creativecommons.org/licenses/by/4.0/).

Introduction

Knee osteoarthritis (KOA) is a prevalent degenerative joint disease characterized by chronic pain and functional impairment, imposing a substantial socioeconomic burden worldwide [1]. Traditionally, KOA was predominantly viewed as a disease of articular cartilage degeneration. However, recent advances have redefined KOA as a "whole-joint" disease involving the cartilage, subchondral bone (SCB), synovium, and other joint tissues [2,3]. Among these components, abnormal remodeling of the SCB has emerged not only as a consequence of cartilage degeneration but also as an active contributor to osteoarthritis (OA) progression [4,5]. Accumulating evidence indicates that metabolic dysregulation within the SCB microenvironment can promote catabolic activity and hypertrophic degeneration in overlying chondrocytes through pathological bone–cartilage crosstalk, ultimately contributing to joint degeneration [6,7]. Therefore, elucidating the regulatory role of the SCB microenvironment and identifying effective intervention strategies are important for the development of

disease-modifying osteoarthritis drugs (DMOADs).

Despite the growing recognition of the SCB as an important therapeutic target in OA, current clinical interventions remain limited [8]. Routine conservative treatments, such as nonsteroidal anti-inflammatory drugs (NSAIDs), mainly provide symptomatic relief but do not reverse the underlying structural degeneration [9]. Although intra-articular injections can increase local drug concentrations, their efficacy is limited by rapid synovial fluid clearance, resulting in transient drug retention and insufficient bioavailability [10,11]. Moreover, the dense anatomical architecture of the SCB may restrict drug penetration into deeper pathological microenvironments [12]. Therefore, developing an *in situ* delivery system capable of local retention, lesion filling, and sustained biochemical modulation within the SCB is a promising strategy for OA treatment [13,14].

To address these challenges in localized delivery, *in situ* crosslinkable biopolymer hydrogels offer distinct therapeutic advantages. Hyaluronic acid (HA), a natural extracellular matrix component of articular cartilage and synovial fluid, exhibits excellent biocompatibility [15]. Through methacrylation, the resulting hyaluronic acid methacrylate (HAMA) hydrogel retains the intrinsic bioactivity of HA while acquiring injectability and photo-crosslinking capability. This *in situ* gelation property allows the hydrogel to fill irregular micro-defects within the SCB and form a stable three-dimensional network after photo-irradiation. Therefore, HAMA hydrogel may provide local retention and structural filling at the lesion site [16,17].

For biochemical modulation of the SCB microenvironment, artemisinin (ART), a natural small-molecule drug, has recently attracted attention for its therapeutic potential in osteoarticular diseases. Previous studies have suggested that ART may exert anti-inflammatory effects and regulate OA-related pathological changes [18,19]. Based on these findings, we hypothesized that integrating the localized delivery capacity of HAMA hydrogel with the biological activity of ART could provide a dual-function system combining physical defect filling with microenvironment modulation. By enabling sustained local release of ART within SCB lesions, this composite system was designed to modulate the aberrant osteoblast phenotype and attenuate pathological osteoblast–chondrocyte communication [20].

To this end, the present study developed an ART-loaded, *in situ* photo-crosslinkable HAMA hydrogel (HAMA-ART) for localized intervention in the SCB. After validating the physicochemical properties and biocompatibility of the hydrogel, *in vitro* co-culture experiments demonstrated that HAMA-ART attenuated aberrant Runt-related transcription factor 2 (*Runx2*) upregulation in OA osteoblasts under non-cytotoxic conditions. This effect was associated with reduced pathological paracrine effects on chondrocytes and improved cartilage matrix metabolic homeostasis. Furthermore, *in situ* implantation in a rat OA model showed that the HAMA-ART system alleviated SCB microstructural deterioration and protected the overlying articular cartilage.

Materials and Methods

Materials

HAMA (100–200 kDa, degree of substitution 60%–70%) was purchased from Shenzhen Shenning Biotechnology Co., Ltd. (Shenzhen, China). The photoinitiator lithium phenyl-2,4,6-trimethylbenzoylphosphinate (LAP, EFL-l2959) was obtained from Engineering for Life (Suzhou, China). ART (A8340, purity > 99.0%) was purchased from Solarbio Science & Technology Co., Ltd. (Beijing, China). Human knee joint specimens were collected from 5 patients undergoing total knee arthroplasty at The Affiliated Hospital of Guizhou Medical University. This study was approved by the Human Research Ethics Committee of The Affiliated Hospital of Guizhou Medical University (Approval No. 2025-272). Prior to sample collection, all patients were fully informed of the study objectives and provided written informed consent.

SCB Morphological Observation and Osteoblast Isolation

Medial sclerotic SCB (OA group) and lateral non-sclerotic SCB (CON group) were harvested from the femoral condyles of the collected specimens [21]. For morphological evaluation, the bone tissues were fixed in electron microscopy fixative, dehydrated, and examined using a scanning electron microscope (SEM, JEOL, JEM-IT800, Japan).

For primary osteoblast isolation, fresh tissues were thoroughly rinsed with sterile phosphate-buffered saline (PBS) to remove surface blood and debris, then minced into 1–2 mm^3 fragments using bone rongeurs. The fragments were initially digested with trypsin in a shaking incubator at 37 °C for 30 min. The solution was then replaced with 1 mg/mL type I collagenase (C8140, Solarbio, Beijing, China) for an additional 5–6 h. The resulting cell suspension was centrifuged at 1200 rpm for 5 min. The cell pellet was resuspended in MEM-α supplemented with 10% fetal bovine serum (FBS) and 1% penicillin–streptomycin, and subsequently seeded into T25 culture flasks. The culture medium was replaced every 2–3 days. The osteoblast (P2–P4) phenotype was verified via Alizarin Red S (G8550, Solarbio, Beijing, China) and alkaline phosphatase (ALP) staining (G1480, Solarbio, Beijing, China). The differential expression of *Runx2* between the CON and OA groups was assessed by Western blotting (WB).

Chondrocyte Isolation and the Effect of Osteoblasts on OA Progression in Chondrocytes

Articular cartilage was harvested from the femoral condyles using sterile scalpels and rinsed with sterile PBS. The cartilage was diced into fragments smaller than 1 mm^3

and subjected to continuous digestion with 1 mg/mL type II collagenase (C8150, Solarbio, Beijing, China) in a shaking incubator at 37 °C for 12 h. The digested suspension was centrifuged at 1200 rpm for 5 min. The isolated primary chondrocytes were resuspended in DMEM/F12 medium containing 10% FBS and 1% penicillin–streptomycin, and seeded into T25 flasks. The medium was refreshed every 2–3 days. Chondrocyte identity was confirmed by Toluidine Blue and Alcian Blue staining. Primary osteoblasts and chondrocytes at P2–P4 were used for subsequent *in vitro* experiments to maintain phenotypic stability and reduce the influence of cellular dedifferentiation during expansion.

To investigate bone–cartilage crosstalk, conditioned medium (CM) were collected from the culture supernatants of CON and OA osteoblasts and applied to the primary chondrocytes. The expression of Type X Collagen (CLOX) and subsequent OA-like phenotypic changes in the chondrocytes were evaluated using WB and immunofluorescence (IF) staining.

Preparation and Characterization of HAMA-ART Hydrogel

ART was pre-dissolved in dimethyl sulfoxide (DMSO, ID9011, Solarbio, Beijing, China) and homogeneously dispersed into a 4% (w/v) HAMA aqueous solution containing 0.5% (w/v) LAP as the photoinitiator. The ART concentrations in the precursor solutions were set at 10, 20, 50, and 100 μM. These solutions were then photo-crosslinked into hydrogels under 365 nm ultraviolet (UV) irradiation. To determine the optimal ART loading concentration, hydrogels were placed in the upper chambers of a Transwell system for non-contact co-culture with osteoblasts in the lower chambers. After 5 days of culture, osteoblast proliferation was quantified using a Cell Counting Kit-8 (CCK-8) assay.

Based on these results, the HAMA-ART precursor solution containing the optimal ART concentration was selected for subsequent experiments, while pure HAMA hydrogel served as the matrix control. After photo-crosslinking, the hydrogels were lyophilized, and their internal microstructure was observed by scanning electron microscopy (SEM). Pore size distribution and porosity were quantified from SEM images using ImageJ software (version 1.54p, National Institutes of Health, Bethesda, MD, USA). The chemical composition and ART incorporation within the HAMA-ART hydrogel were evaluated using Fourier transform infrared spectroscopy (FTIR, Nicolet is5, Thermo Fisher, USA).

To assess the drug release behavior, crosslinked HAMA-ART hydrogels were incubated in release medium at 37 °C. At predetermined time points, the supernatant was collected and replaced with fresh release medium. The released ART was quantified by high-performance liquid chromatography (HPLC, 1220 Infinity II, Agilent, USA) based on a standard calibration curve, and the cumulative release profile was calculated.

For the *in vitro* degradation assay, HAMA and HAMA-ART hydrogels were incubated in PBS containing 50 U/mL hyaluronidase and 0.5% ProClean 150 antimicrobial preservative at 37 °C. At predetermined time points, the hydrogel samples, together with the pre-weighed containers, were dried in an oven and then weighed. The dry weight of the remaining hydrogel was calculated after subtracting the container weight. The mass loss was calculated using the following formula: Mass loss (%) = [(W0 − Wt) / W0] × 100%, where W0 represents the initial dry weight of the hydrogel, and Wt represents the dry weight of the remaining hydrogel at each time point.

Rheological properties of HAMA and HAMA-ART hydrogels were evaluated using a rotational rheometer (MCR 302, Anton Paar, Graz, Austria) by measuring the storage modulus (G′) and loss modulus (G″). Compressive mechanical properties were assessed using a mechanical testing system (QJ211S, Qingji, Shanghai, China), and compressive strength and compressive modulus were calculated from the stress–strain curves.

Biocompatibility Evaluation of HAMA-ART Hydrogel

HAMA and HAMA-ART hydrogels were co-cultured with osteoblasts to evaluate cytocompatibility. Cell viability was assessed using a Live/Dead viability/cytotoxicity assay kit. Following co-culture, the cells were stained and imaged using a fluorescence microscope (Axio Observer, Carl Zeiss, Germany). The proportion of viable cells was quantified utilizing ImageJ software.

For the hemocompatibility assay, fully crosslinked HAMA and HAMA-ART hydrogel samples were immersed in sterile PBS and incubated in a shaking incubator at 37 °C for 48 h to obtain the material extract. Normal saline and 0.5% Triton X-100 solution were utilized as negative and positive controls, respectively. Each extract/control solution was mixed with a diluted red blood cell suspension and incubated at 37 °C for 2 h. Subsequently, the mixtures were centrifuged, the supernatants were collected, and the optical density (OD) was measured at 540 nm using a microplate reader (SYNERGY H1, Bio Tek, USA) to calculate the hemolysis ratio.

Effects of HAMA-ART Hydrogel on Osteoblasts and OA Chondrocytes

To investigate the modulatory effects of the material, photo-crosslinked HAMA-ART hydrogels were placed in Transwell inserts and co-cultured with OA osteo-blasts for 72 h. OA osteoblasts cultured without hydrogel treatment served as the OA control group, while pure HAMA hydrogels served as the matrix control. Following the intervention, osteoblasts were harvested, and total protein was extracted using radioimmunoprecipitation assay lysis buffer (RIPA) lysis buffer supplemented with protease and phosphatase inhibitors. The expression level of *Runx2*

was quantified via WB. Furthermore, the CM from these treated osteoblast cultures were collected and subsequently used to culture primary chondrocytes for an additional 72 h. To assess the downstream effects on cartilage matrix metabolism, the expression levels of *COLX*, Type II Collagen Alpha 1 (*COL2A1*), and Matrix Metalloproteinase 13 (*MMP13*) in the treated chondrocytes were evaluated utilizing both WB and IF staining.

IF Staining

Cells were seeded onto coverslips in 6-well plates and incubated until adherence. Following the respective treatments, cells were gently washed three times with PBS, fixed with 4% paraformaldehyde at room temperature (RT) for 15 min, and washed again. Permeabilization was performed using 0.3% Triton X-100 (in PBS) at RT for 10–15 min. Subsequently, cells were blocked with 5% bovine serum albumin (BSA) at RT for 1 h to prevent non-specific binding. After removing the blocking solution, the cells were incubated with diluted primary antibodies in a humidified chamber at 4 °C overnight (Antibody information and dilution ratio details are listed in **Supplementary Table 1**). The following day, the samples were equilibrated to RT for 30 min, washed three times with PBST (PBS with Tween-20), and incubated with species-specific fluorophore-conjugated secondary antibodies at RT in the dark for 1 h. After thorough PBST washing, the actin cytoskeleton was stained with FITC-conjugated phalloidin (1:80). Finally, nuclei were counterstained with DAPI for 2 min in the dark. The coverslips were rinsed to remove background fluorescence and mounted onto glass slides using an anti-fade mounting medium. Images were subsequently captured using a fluorescence microscope (Axio Imager, Carl Zeiss, Germany).

Western Blotting

After completing the respective interventions in 6-well plates, total cellular proteins were extracted using RIPA lysis buffer, and protein concentrations were determined utilizing a BCA protein assay kit. Equal amounts of protein (30 μg per lane) were separated by SDS-PAGE and transferred onto PVDF membranes. The membranes were blocked with a protein-free rapid blocking buffer at RT for 1 h, followed by overnight incubation at 4 °C with specific primary antibodies (Antibody information and dilution ratio details are listed in **Supplementary Table 1**). The next day, the membranes were washed thoroughly with TBST (Tris-buffered saline with Tween-20) and incubated with HRP-conjugated secondary antibodies at RT for 1.5 h. After final TBST washes, the target protein bands were visualized using an enhanced chemiluminescence (ECL) detection system (ChemiScope 6000, CLINX, Shanghai, China). Images were acquired and analyzed via densitometry using ImageJ software.

Establishment of Sprague-Dawley (SD) Rat KOA Model by Destabilization of the Medial Meniscus (DMM) Surgery

Twenty-two male SD rats (weighing approximately 250 g), purchased from Tianqin Co., Ltd. (Changsha, China), were randomly assigned to the Sham group (n = 5) and DMM model group (n = 17). General anesthesia was induced and maintained via isoflurane inhalation. The surgical site of the right knee was shaved, disinfected, and draped, supplemented by local infiltration anesthesia using lidocaine. In the model group, a 1.5-cm longitudinal incision was made medial to the patella. The patella was laterally dislocated to expose the joint cavity, and the anterior meniscotibial ligament of the medial meniscus was transected to establish the DMM model. In the Sham group, the joint cavity was exposed identically, but the meniscus was left intact. The joint capsule and skin were sutured layer by layer and disinfected. Postoperatively, all rats were housed under standard pathogen-free conditions with ad libitum access to food and water. To prevent infection and manage pain, intramuscular injections of penicillin and parecoxib were administered for 5 consecutive days. All animals recovered uneventfully. Four weeks post-surgery, two rats from the model group were randomly euthanized for pathological sectioning to verify the successful establishment of OA (**Supplementary Fig. 1**). The remaining 15 rats proceeded to the subsequent bone defect creation and hydrogel implantation phase.

In situ Implantation of HAMA-ART Hydrogel into SCB

Rats with successfully established DMM models were re-anesthetized. The original incision was re-opened, and the knee was maximally flexed to expose the medial femoral condyle. A cylindrical focal bone defect (3 mm in diameter and 2–3 mm in depth) was meticulously created within the cancellous bone region using a medical bone drill. Bone debris was flushed out via repeated sterile saline irrigation, and the defect site was dried using sterile cotton swabs. Subsequently, 30 μL of the pre-formulated hydrogel precursor solution (HAMA or HAMA-ART) was precisely injected into the defect via a micropipette to ensure complete cavity filling. The hydrogel was then *in situ* photocrosslinked and fully cured using local 365 nm UV irradiation (**Supplementary Fig. 2**). For the vehicle control (Saline group), an equal volume of sterile saline was injected into the defect. For the Sham group, the medial femoral skin was incised and sutured without creating a bone defect.

Postoperative Radiographic Evaluation of the Knee Joint

At 8 weeks post-implantation, all SD rats (n = 5 per group) were euthanized. The intact knee joints were harvested, fixed in 4% paraformaldehyde (PFA) at RT for 48 h, and subsequently transferred to 70% ethanol. The fixed joints were secured along their longitudinal axis in scanning tubes and subjected to high-resolution Micro-CT scanning

(VNC-102, Pingseng, Jiangsu, China). The acquired 2D tomographic slices were imported into the system's integrated software to generate 3D spatial reconstructions of the tibial and femoral compartments. Quantitative analysis of the SCB microarchitecture was performed by an investigator blinded to the treatment groups, evaluating key parameters including bone volume fraction (BV/TV), trabecular thickness (Tb.Th), and trabecular separation (Tb.Sp).

Histopathological and IF Staining of Joint Sections

Following Micro-CT scanning, the fixed specimens were decalcified in 10% EDTA solution on a shaker at 37 °C for approximately 4 weeks, with the solution refreshed every 3 days. Upon confirmation of complete decalcification via needle puncture, the samples underwent routine gradient ethanol dehydration, xylene clearing, and paraffin embedding. Serial 5 μm thick sagittal sections were cut and baked onto glass slides.

For histopathological evaluation, deparaffinized and rehydrated sections (n = 5 per group) were stained with Hematoxylin-Eosin (H&E) and Safranin O-Fast Green. Cartilage integrity, cellular arrangement, and proteoglycan content were examined using bright-field microscopy. Cartilage thickness in the weight-bearing area of the medial tibial plateau was quantified using ImageJ software. Additionally, structural damage in Safranin O-stained sections was independently evaluated by two blinded researchers using the modified Mankin scoring system.

For *in situ* IF analysis, rehydrated sections underwent enzymatic antigen retrieval using a pepsin solution. After blocking with 5% BSA for 1 h at RT, the sections were incubated overnight at 4 °C with primary antibodies targeting *COL2A1*, *MMP13*, or *Runx2*. Following PBS washes, the sections were incubated with corresponding fluorophore-conjugated secondary antibodies in the dark for 1 h at RT. Nuclei were counterstained with DAPI, and the slides were mounted. Images were acquired using a fluorescence microscope, and the mean fluorescence intensities of *COL2A1* and *MMP13* were quantified using ImageJ software.

Statistical Analysis

All quantitative data are presented as the mean ± standard deviation from at least three independent experiments ($n \geq 3$). Statistical analyses and data visualization were performed using GraphPad Prism 10.0 software (GraphPad Software, LLC, Boston, MA, USA). Pairwise comparisons were analyzed using the two-tailed Student's *t*-test, while comparisons among three or more groups were conducted using one-way analysis of variance (ANOVA) followed by Tukey's post-hoc test. Normality of the data was assessed using the Shapiro-Wilk test. Non-parametric data were analyzed using the Kruskal-Wallis test. $p < 0.05$ was considered statistically significant.

Results

Morphological Characterization of SCB and Runx2 Expression in Osteoblasts

We first evaluated morphological differences between the sclerotic medial region and the relatively non-sclerotic lateral region of femoral condyles from OA patients. Gross observation showed apparent densification and hardening in the medial region. SEM further showed that the lateral region retained a relatively porous trabecular structure, whereas the medial region exhibited trabecular thickening and fusion, resulting in a dense plate-like microstructure (Fig. 1**A**).

Primary osteoblasts were subsequently isolated from SCB tissues. *In vitro*, the adherent cells exhibited spindle-shaped or polygonal morphologies with a characteristic whirlpool-like growth pattern. Alizarin Red S (ARS) staining showed calcified nodule formation, while ALP staining confirmed osteogenic activity (Fig. 1**B**). Western blot analysis showed that *Runx2* protein levels were significantly higher in osteoblasts from the sclerotic region (OA group) than in those from the relatively non-sclerotic region (CON group) ($p < 0.01$; Fig. 1**C,D**).

Chondrocyte Characterization and Osteoblast-Driven Paracrine Effects on Cartilage Degeneration

Primary articular chondrocytes exhibited typical polygonal or short spindle-like morphologies *in vitro*, forming a cobblestone-like pattern at high confluence. Toluidine Blue and Alcian Blue staining confirmed the secretion of proteoglycans and acidic mucopolysaccharides, verifying the chondrocyte phenotype (Fig. 2**A**).

To evaluate osteoblast–chondrocyte paracrine communication, chondrocytes were treated with CM derived from either CON or OA osteoblasts. Western blot analysis showed that CM from OA osteoblasts significantly reduced *COL2A1* expression and increased *MMP13* and *COLX* expression in chondrocytes compared with CM from CON osteoblasts (Fig. 2**B–E**). Immunofluorescence staining showed a similar trend, with decreased *COL2A1* expression and increased *MMP13* intensity in OA CM-treated chondrocytes (Fig. 2**F–I**). These findings suggest that OA subchondral osteoblast-derived soluble factors may promote catabolic and hypertrophic changes in chondrocytes.

Characterization and Optimization of HAMA-ART Hydrogels

The chemical structure of HAMA, which served as the hydrogel matrix, is shown in Fig. 3**A**. ART was dissolved in DMSO and then incorporated into the HAMA precursor solution to prepare the HAMA-ART hydrogel (Fig. 3**B**). To determine the optimal ART-loading concentration, hydrogels containing different ART concentrations were co-cultured with osteoblasts. CCK-8 results showed that 100 μM ART significantly inhibited osteoblast proliferation, whereas 50 μM maintained favorable cytocompati-

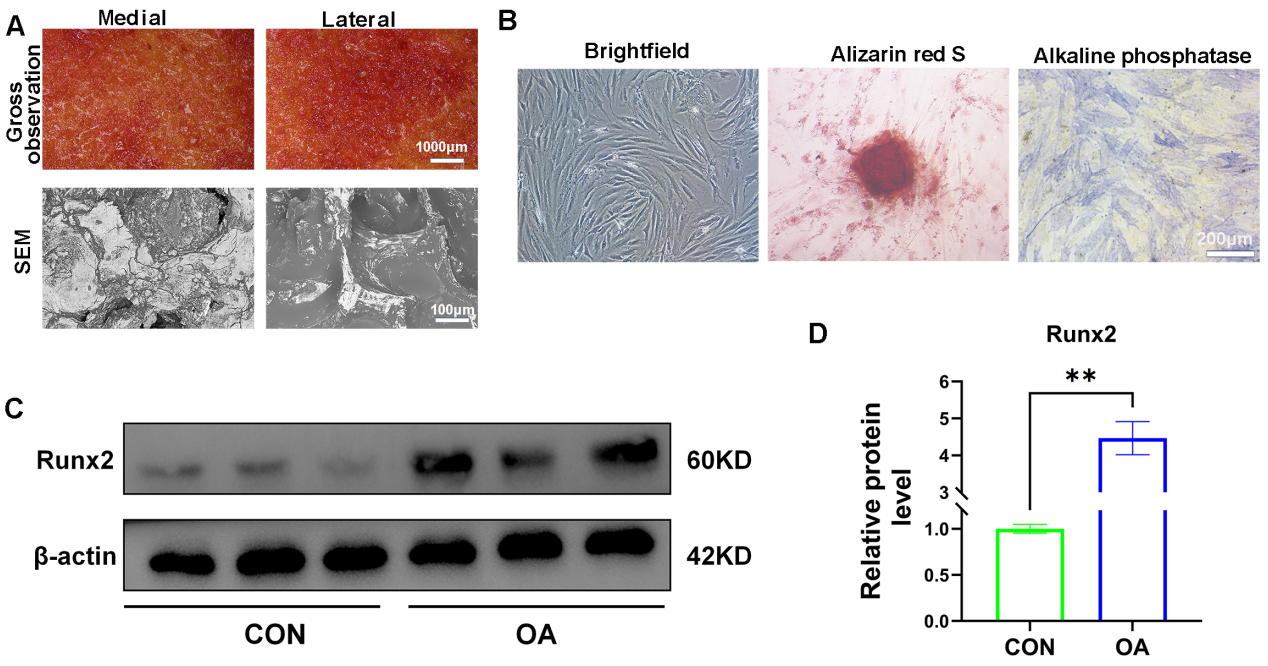


Fig. 1. Morphological differences in subchondral bone between sclerotic and non-sclerotic regions in OA patients and *Runx2* expression in osteoblasts. (**A**) Macroscopic and scanning electron microscopy (SEM) images of subchondral bone from the medial sclerotic and lateral non-sclerotic regions of the femoral condyle in osteoarthritis (OA) patients. (**B**) Light microscopy morphology of primary osteoblasts isolated from subchondral bone, along with Alizarin Red S (ARS) and alkaline phosphatase (ALP) staining to confirm the osteogenic phenotype and calcified nodule formation. (**C,D**) Representative Western blot bands and quantitative analysis of the osteogenic transcription factor *Runx2* in osteoblasts isolated from non-sclerotic (CON group) and sclerotic (OA group) subchondral bone (n = 3, $^{**}p < 0.01$). Image analysis was performed using ImageJ, quantitative graphs were generated using GraphPad Prism 10.0, and the figure was assembled using Adobe Photoshop 2021 (Adobe Inc., San Jose, CA, USA).

bility (Fig. 3**C**). Therefore, 50 μM was selected as the ART-loading concentration for subsequent experiments.

Macroscopic observation showed that both HAMA and HAMA-ART precursors were transparent and flowable before crosslinking. After 365 nm UV irradiation, both groups underwent sol–gel transition and formed stable hydrogels (Fig. 3**D**). SEM imaging showed that both lyophilized HAMA and HAMA-ART hydrogels exhibited porous network structures (Fig. 3**E**). Quantitative analysis showed that the mean pore size decreased from 104.3 $\pm$ 71.03 μm in the HAMA group to 68.05 $\pm$ 37.40 μm in the HAMA-ART group after ART incorporation, while the total porosity showed no significant difference between the two groups (Fig. 3**F**). These results suggest that ART incorporation affected the pore size distribution of the HAMA hydrogel while largely preserving its overall porosity.

FTIR analysis was performed to evaluate ART incorporation within the HAMA hydrogel matrix. The HAMA-ART composite displayed characteristic absorption peaks corresponding to both HAMA, including O–H stretching at 3334 cm^{-1} and C=O stretching at 1653 cm^{-1}, and ART, including C=O stretching at 1743 cm^{-1} and C–O–C stretching at 1030 cm^{-1} (Fig. 3**G**). No obvious new absorption peaks or marked peak shifts were observed after ART loading, suggesting that ART was mainly incorporated into the HAMA hydrogel network through physical encapsulation rather than the formation of new covalent bonds.

The *in vitro* release assay showed that ART was gradually released from the HAMA-ART hydrogel over the 24-day observation period, indicating a sustained release profile (Fig. 3**H**). In addition, the degradation assay showed a progressive increase in mass loss over time in both HAMA and HAMA-ART hydrogels, indicating that the hydrogels were degradable under hyaluronidase-containing conditions (Fig. 3**I**).

In addition, the mechanical properties of HAMA and HAMA-ART hydrogels were further evaluated. Rheological analysis showed that both hydrogels exhibited typical gel-like behavior after photo-crosslinking, with the storage modulus (G′) higher than the loss modulus (G″). Quantitative analysis showed no significant differences in either G′ or G″ between the HAMA and HAMA-ART groups, indicating that ART incorporation did not markedly affect the viscoelastic properties of the HAMA hydrogel (**Supplementary Fig. 3A–C**). Compressive testing further showed that ART incorporation altered the compressive mechanical response of the HAMA hydrogel. Compared with HAMA, HAMA-ART exhibited a lower com-

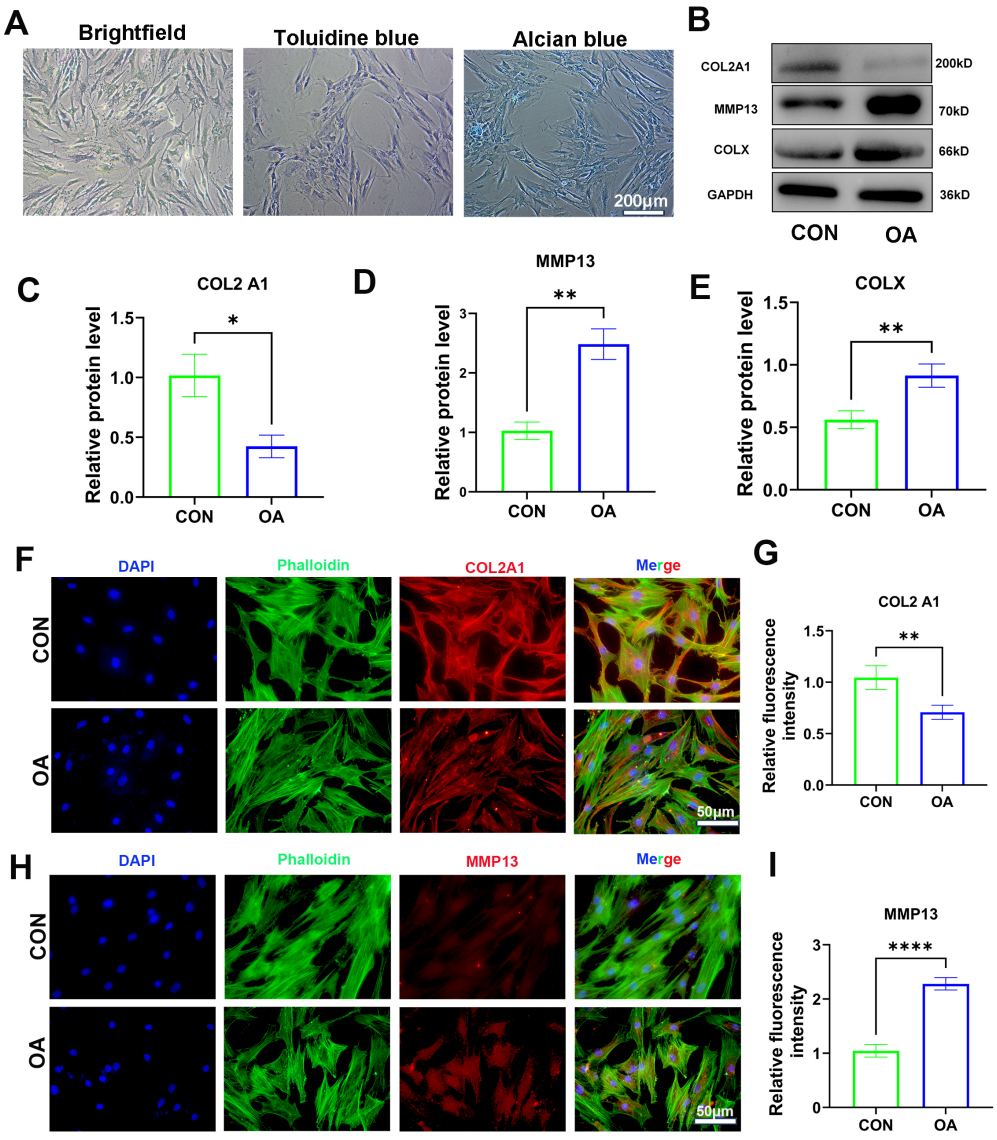


Fig. 2. Paracrine effects of OA subchondral osteoblasts on chondrocyte matrix metabolism and hypertrophy. (**A**) Light microscopy images of isolated primary chondrocytes, with Toluidine Blue and Alcian Blue staining confirming the chondrogenic phenotype. (**B–E**) Representative Western blot bands and quantification of the anabolic marker *COL2A1*, hypertrophic marker *COLX*, and catabolic enzyme *MMP13* in chondrocytes treated with conditioned medium (CM) from normal (CON group) or OA osteoblasts (OA group) (n = 3). (**F,G**) Representative immunofluorescence images and fluorescence intensity quantification of *COL2A1* in chondrocytes (n = 5). (**H,I**) Representative immunofluorescence images and fluorescence intensity quantification of *MMP13* in chondrocytes (n = 5) (*$p <$ 0.05, **$p < 0.01$, ****$p < 0.0001$). Image analysis was performed using ImageJ, quantitative graphs were generated using GraphPad Prism 10.0, and the figure was assembled using Adobe Photoshop 2021 (Adobe Inc., San Jose, CA, USA).

pressive strength but a higher compressive modulus, indicating increased initial compressive stiffness but reduced ultimate compressive resistance (**Supplementary Fig. 3D–F**). These results suggest that ART loading modified the internal network response of the hydrogel under compression.

Biocompatibility of the HAMA and HAMA-ART Hydrogel

To evaluate *in vitro* biosafety, osteoblasts were co-cultured with HAMA and HAMA-ART hydrogels and assessed by live/dead staining on days 1 and 5. On day 1, cells in all groups predominantly exhibited green fluorescence, with only minimal red fluorescence, indicating good cell viability (Fig. 4**A**). Quantitative analysis showed that cell viability exceeded 90% in all groups, with no significant differences among the groups (Fig. 4**B**). By day 5, cell density increased, while the proportion of dead cells remained low (Fig. 4**C**). Cell viability remained above 90% across all groups (Fig. 4**D**).

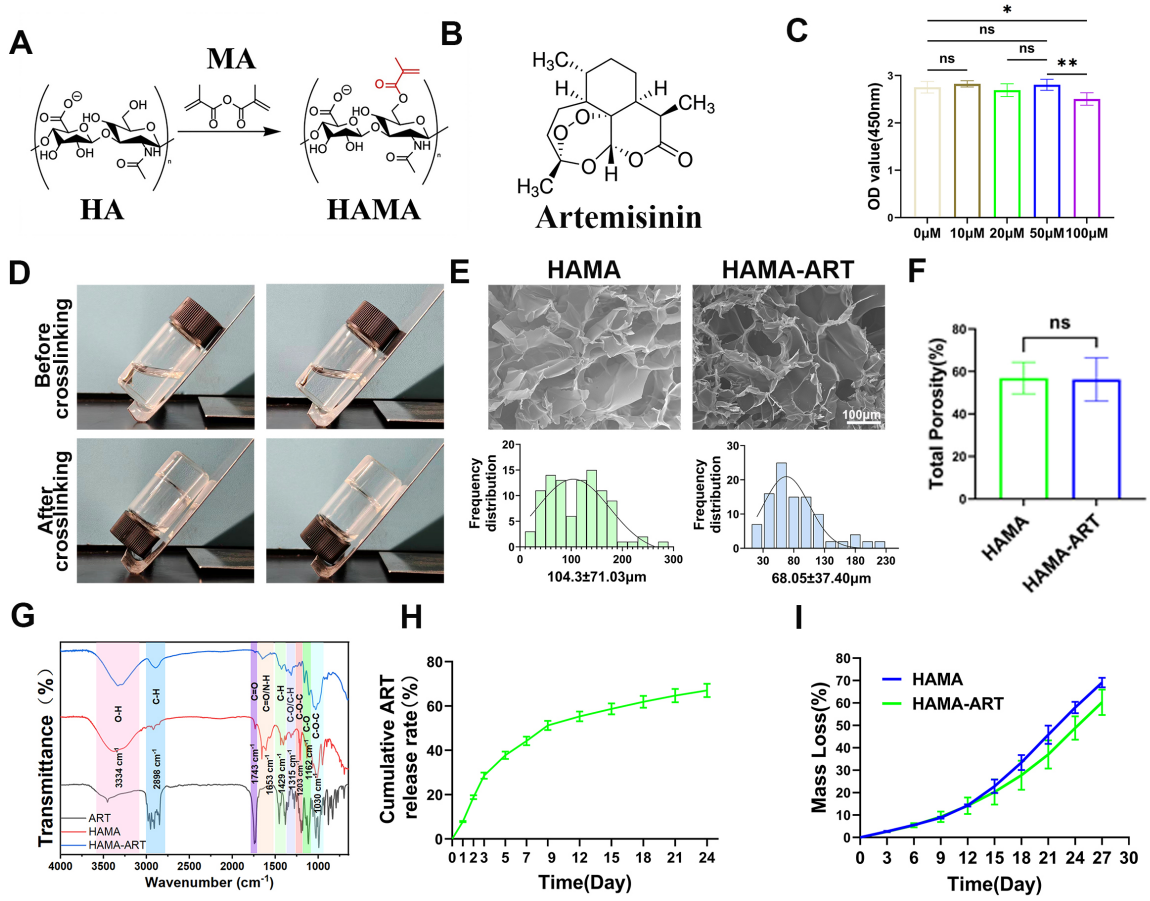


Fig. 3. Preparation and characterization of *in situ* photo-crosslinked HAMA-ART hydrogels. (**A**) Chemical structure and synthesis schematic of HAMA. (**B**) Chemical structure of ART. (Both structures were drawn using Photoshop 2021 based on structural information provided by the manufacturer). (**C**) Effects of varying ART loading concentrations on osteoblast proliferation measured by CCK-8 assay. (**D**) Macroscopic images of HAMA and HAMA-ART hydrogels before and after 365 nm UV irradiation. (**E**) SEM images and pore size distribution of lyophilized HAMA and HAMA-ART hydrogel networks. (**F**) Total porosity of HAMA and HAMA-ART hydrogels. (**G**) FTIR spectra of the HAMA hydrogel, ART, and HAMA-ART hydrogel. (**H**) *In vitro* ART release profile from HAMA-ART hydrogel. (**I**) *In vitro* degradation profiles of HAMA and HAMA-ART hydrogels. Data are presented as mean ± standard deviation. *$p < 0.05$; **$p < 0.01$. ns, not significant. The chemical structures in panels A and B were drawn using Adobe Photoshop 2021 (Adobe Inc., San Jose, CA, USA) based on structural information provided by the manufacturers. Quantitative graphs were generated using GraphPad Prism 10.0, and the figure was assembled using Adobe Photoshop 2021.

An *in vitro* hemolysis assay was further performed to evaluate hemocompatibility. The supernatants of the HAMA, HAMA-ART, and saline groups remained clear, with intact red blood cell sedimentation, whereas the Triton X-100 group showed obvious hemolysis (Fig. 4**E**). Quantitative analysis at 540 nm showed that the hemolysis levels in the HAMA and HAMA-ART groups were negligible and not significantly different from the saline group, but were significantly lower than those in the Triton X-100 group ($p < 0.0001$; Fig. 4**F**). These results indicate that both HAMA and HAMA-ART hydrogels had favorable cytocompatibility and hemocompatibility. They also suggest that the subsequent *Runx2* downregulation observed in HAMA-ART-treated osteoblasts was unlikely to be caused by non-specific cytotoxicity.

HAMA-ART Hydrogel Downregulates Runx2 in OA Osteoblasts and Modulates Osteoblast–Chondrocyte Paracrine Effects In vitro

To evaluate the modulatory effect of HAMA-ART on OA osteoblasts, hydrogels were co-cultured with OA osteoblasts. Western blot analysis showed that HAMA-ART significantly reduced *Runx2* expression in OA osteoblasts compared with both the untreated OA control and HAMA-only groups (Fig. 5**A,B**). The HAMA-only group did not induce an equivalent decrease in *Runx2* expression, suggesting that the observed *Runx2* reduction was not simply caused by the HAMA matrix or hydrogel-mediated changes in the culture environment (Fig. 5**A,B**).

To assess the downstream paracrine effects on chondrocytes, primary chondrocytes were treated with CM derived from these osteoblast cultures. Western blot analy-

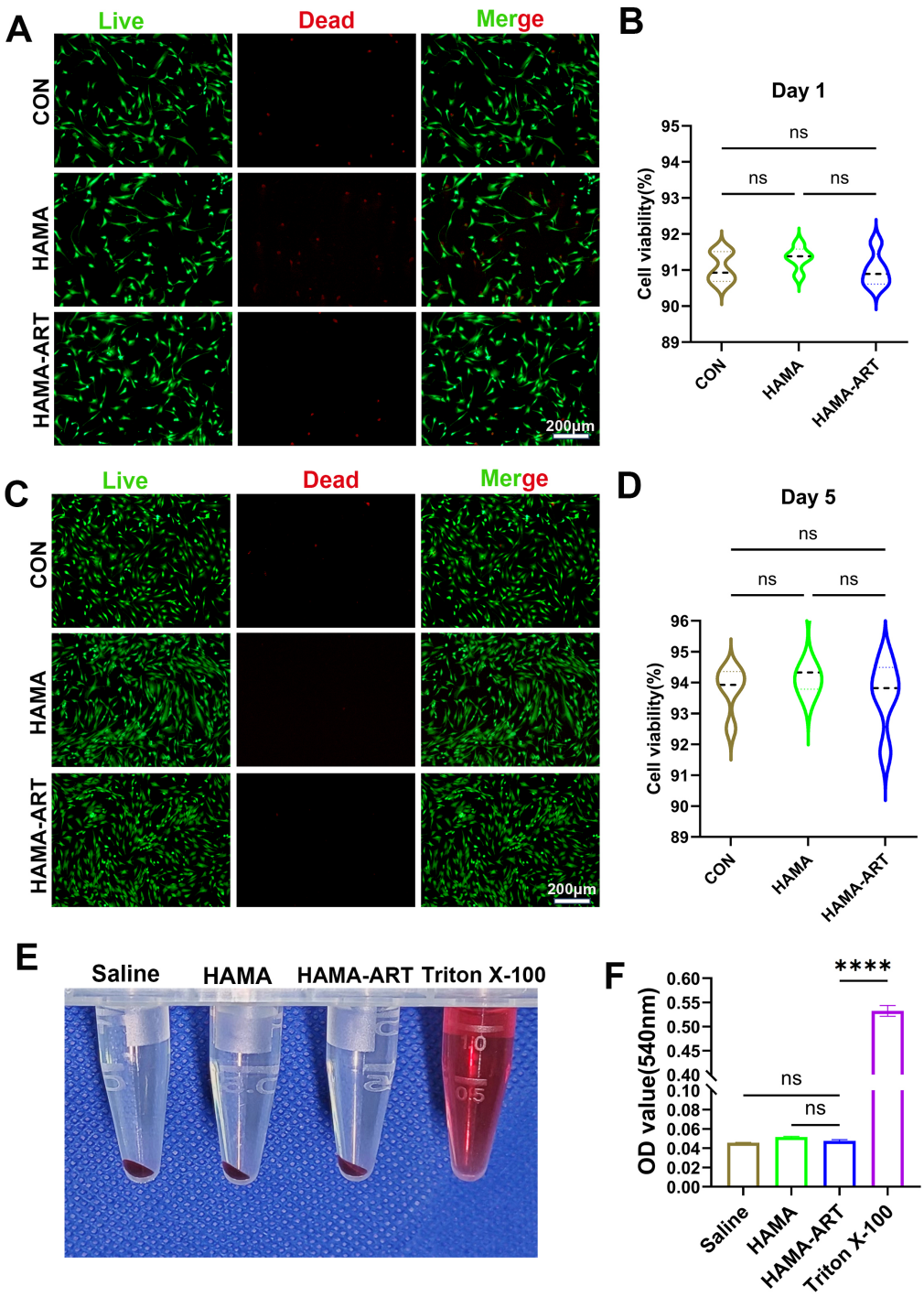


Fig. 4. ***In vitro*** **biocompatibility of HAMA and HAMA-ART hydrogels.** (**A–D**) Representative Live/Dead staining images and quantification of osteoblast viability following co-culture with pure HAMA and HAMA-ART hydrogels on days 1 and 5 (live: green; dead: red; n = 5). (**E,F**) Macroscopic images of the hemolysis assay and quantification of absorbance at 540 nm (n = 5). ****$p < 0.0001$. ns, not significant. Image analysis was performed using ImageJ, quantitative graphs were generated using GraphPad Prism 10.0, and the figure was assembled using Adobe Photoshop 2021 (Adobe Inc., San Jose, CA, USA).

sis showed that CM from HAMA-ART-treated osteoblasts significantly reduced the expression of the hypertrophic marker *COLX* in chondrocytes (Fig. 5**C,D**). IF (Fig. 5**E–H**) and Western blot analysis (Fig. 5**I–K**) further showed that this HAMA-ART-modulated CM preserved *COL2A1* expression and reduced *MMP13* expression compared with CM from untreated OA osteoblasts. These findings suggest that HAMA-ART attenuated the adverse paracrine effects of OA osteoblasts on chondrocytes, which was associated with reduced aberrant *Runx2* expression in OA osteoblasts.

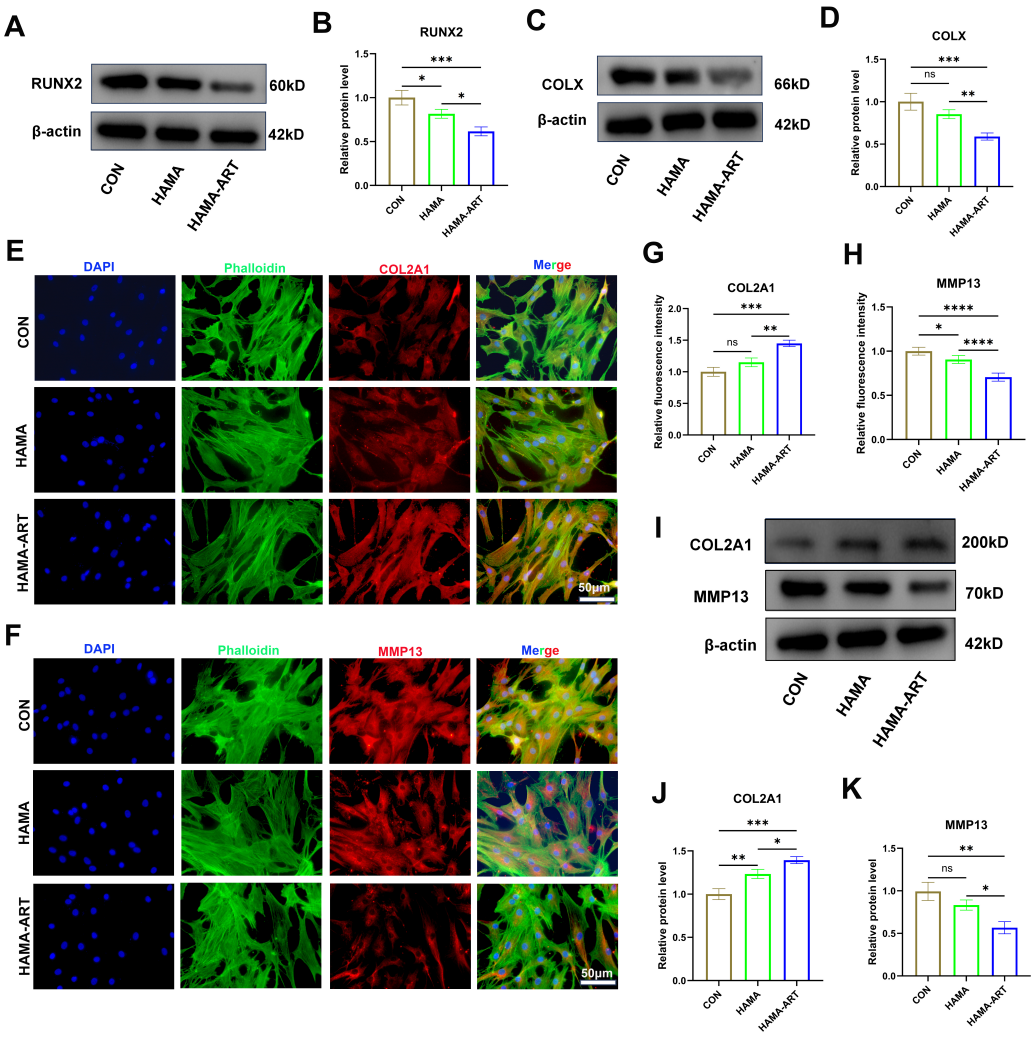


Fig. 5. HAMA-ART downregulates *Runx2* in OA osteoblasts and modulates osteoblast–chondrocyte paracrine effects *in vitro*. (**A,B**) Representative Western blot bands and quantification of *Runx2* in OA osteoblasts following hydrogel intervention (n = 3). (**C,D**) Western blot analysis and quantification of *COLX* in chondrocytes cultured with CM from treated osteoblasts (n = 3). (**E–H**) Representative immunofluorescence images and fluorescence intensity quantification of *COL2A1* and *MMP13* in chondrocytes (n = 5). (**I–K**) Western blot analysis and quantification of *COL2A1* and *MMP13* in chondrocytes (n = 3). *$p < 0.05$; **$p < 0.01$; ***$p < 0.001$; ****$p < 0.0001$. ns, not significant. Image analysis was performed using ImageJ, quantitative graphs were generated using GraphPad Prism 10.0, and the figure was assembled using Adobe Photoshop 2021 (Adobe Inc., San Jose, CA, USA).

HAMA-ART Hydrogels Attenuate Pathological SCB Remodeling In vivo

To evaluate the *in vivo* protective effect of the localized HAMA-ART delivery system, Micro-CT scanning was performed on rat knee joints 8 weeks post-implantation. Three-dimensional reconstructions and two-dimensional coronal sections showed that the Saline and HAMA groups exhibited obvious osteophyte formation, irregular joint contours, and trabecular disruption. In contrast, the HAMA-ART group showed reduced osteophyte formation, better preservation of condylar morphology, and a relatively more continuous subchondral trabecular structure (Fig. 6**A**).

Quantitative analysis of the subchondral cancellous bone further supported these morphological observations. Compared with the Saline and HAMA groups, the HAMA-ART group showed increased bone volume fraction (BV/TV) and trabecular thickness (Tb.Th), together with reduced trabecular separation (Tb.Sp) (Fig. 6**B–D**). These results suggest that localized HAMA-ART intervention attenuated OA-associated SCB microstructural deterioration.

In situ HAMA-ART Implantation Mitigates Articular Cartilage Degeneration

To assess the chondroprotective effects of the HAMA-ART hydrogel, knee joints harvested 8 weeks post-implantation were evaluated by H&E and Safranin O-Fast Green staining. H&E staining showed a smooth cartilage surface with organized chondrocyte distribution in the Sham group. In contrast, the Saline and HAMA groups ex-

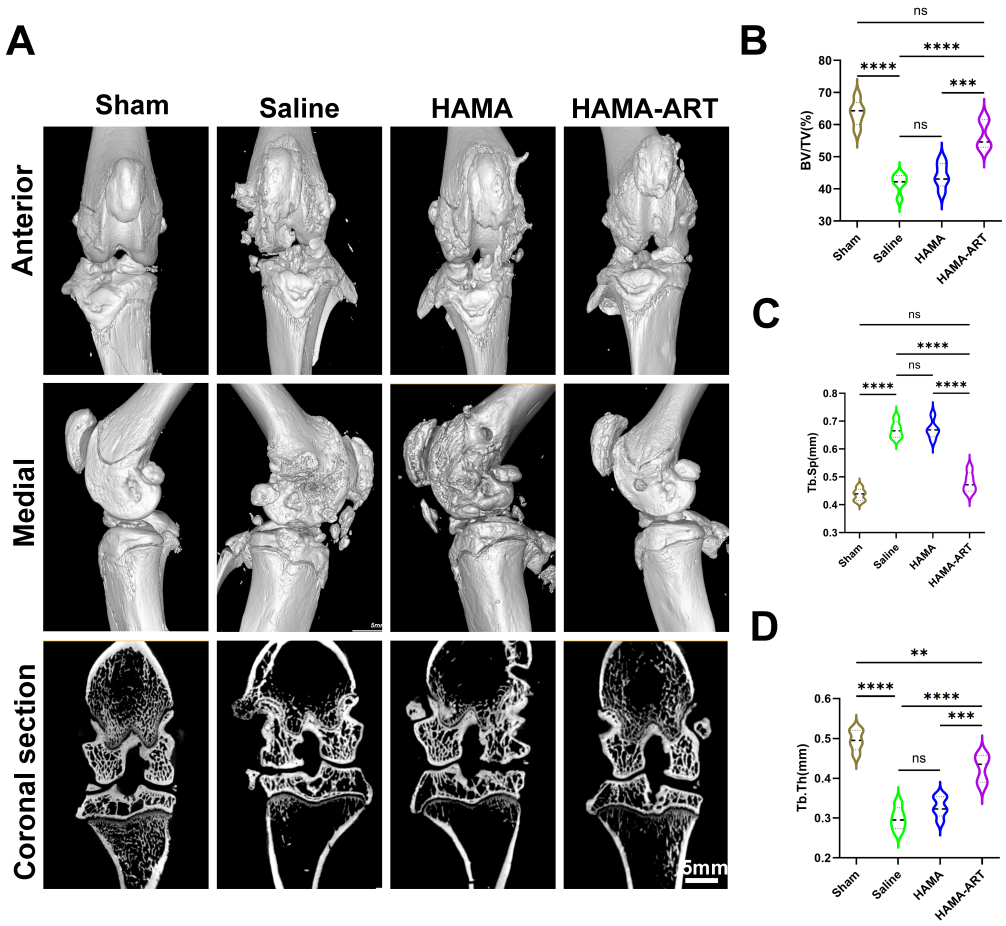


Fig. 6. Micro-CT evaluation of subchondral bone microarchitecture 8 weeks post-implantation. (**A**) 3D Micro-CT reconstructions of rat knee joints 8 weeks post-implantation in the DMM model. (**B–D**) Quantification of subchondral bone microstructural parameters in the medial femoral condyle: bone volume fraction (BV/TV), trabecular separation (Tb.Sp), and trabecular thickness (Tb.Th) (n = 5, $^{**}p < 0.01$, $^{***}p < 0.001$, $^{****}p < 0.0001$. ns, no significant difference). Quantitative graphs were generated using GraphPad Prism 10.0, and the figure was assembled using Adobe Photoshop 2021 (Adobe Inc., San Jose, CA, USA).

hibited cartilage thinning, surface fibrillation, and chondrocyte loss. The HAMA-ART group maintained a relatively intact cartilage surface with better preserved cellular organization and cartilage thickness (Fig. 7**A**).

Safranin O staining showed marked proteoglycan loss in the cartilage of the Saline and HAMA groups, whereas the HAMA-ART group retained stronger red staining, indicating better preservation of cartilage matrix (Fig. 7**B**). Quantification using the modified Mankin score showed more severe cartilage degeneration in the Saline and HAMA groups, which was alleviated by HAMA-ART treatment (Fig. 7**C**). In addition, relative cartilage thickness was better preserved in the HAMA-ART group than in the Saline and HAMA groups (Fig. 7**D**). These histological findings suggest that localized subchondral HAMA-ART implantation mitigated cartilage structural deterioration and matrix loss.

To further evaluate whether HAMA-ART modulated *Runx2* expression *in vivo*, IF staining was performed in SCB sections. Compared with the Saline and HAMA groups, the HAMA-ART group showed reduced *Runx2* fluorescence intensity in the SCB region, which was consistent with the *in vitro* findings. These results indicate that HAMA-ART implantation was associated with attenuation of aberrant *Runx2* expression in the OA SCB microenvironment (**Supplementary Fig. 4**).

HAMA-ART Modulates Cartilage Matrix Metabolism In vivo

To evaluate the *in vivo* effect of HAMA-ART on cartilage matrix metabolism, IF analysis was performed. In the Sham group, the anabolic marker *COL2A1* showed strong fluorescence, whereas its expression was reduced in the Saline and HAMA groups. After HAMA-ART treatment, *COL2A1* fluorescence intensity was partially preserved compared with the Saline and HAMA groups (Fig. 8**A,C**).

In contrast, *MMP13* fluorescence intensity was increased in the Saline and HAMA groups, indicating en-

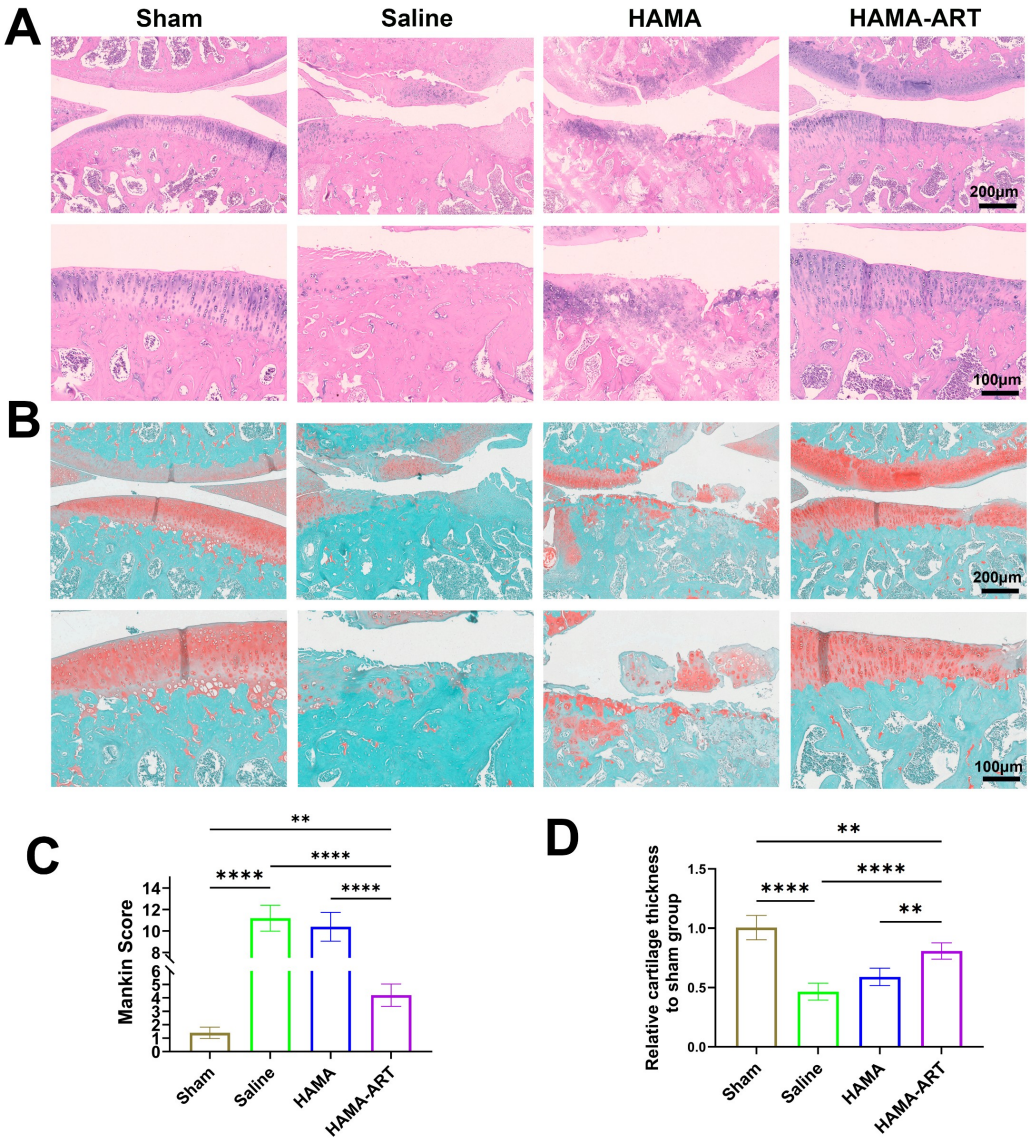


Fig. 7. Histopathological evaluation of the chondroprotective effects of subchondral HAMA-ART implantation. (**A,B**) Representative H&E and Safranin O-Fast-Green stained sections of rat knee joints. (**C**) Modified Mankin scores based on Safranin O staining (n = 5). (**D**) Relative thickness of the articular cartilage layer in the medial weight-bearing area (n = 5) (**$p < 0.01$, ****$p < 0.0001$). Image analysis was performed using ImageJ, quantitative graphs were generated using GraphPad Prism 10.0, and the figure was assembled using Adobe Photoshop 2021 (Adobe Inc., San Jose, CA, USA).

hanced matrix catabolism. HAMA-ART treatment reduced *MMP13* expression compared with the Saline and HAMA groups (Fig. 8**B,D**). These findings suggest that targeted subchondral HAMA-ART intervention helped maintain cartilage matrix metabolic balance by preserving *COL2A1* expression and reducing *MMP13* expression.

Discussion

Conventional clinical interventions for KOA mainly focus on symptomatic relief or the management of late-stage cartilage degeneration, but they often fail to address pathological remodeling within the SCB microenvironment [22,23]. In addition, rapid synovial clearance and the dense anatomical structure of the SCB limit the local retention and penetration of free therapeutic agents [24,25]. To address these challenges, the present study developed an *in situ* photo-crosslinkable HAMA-ART hydrogel for localized modulation of the SCB microenvironment. *In vitro*, HAMA-ART attenuated aberrant *Runx2* upregulation in OA subchondral osteoblasts under non-cytotoxic conditions. Conditioned medium-transfer experiments further suggested that HAMA-ART treatment reduced the adverse soluble factor-mediated paracrine effects of OA osteoblasts on chondrocytes, as reflected by decreased catabolic and hypertrophic responses. *In vivo*, localized HAMA-ART implantation alleviated OA-associated SCB microstruc-

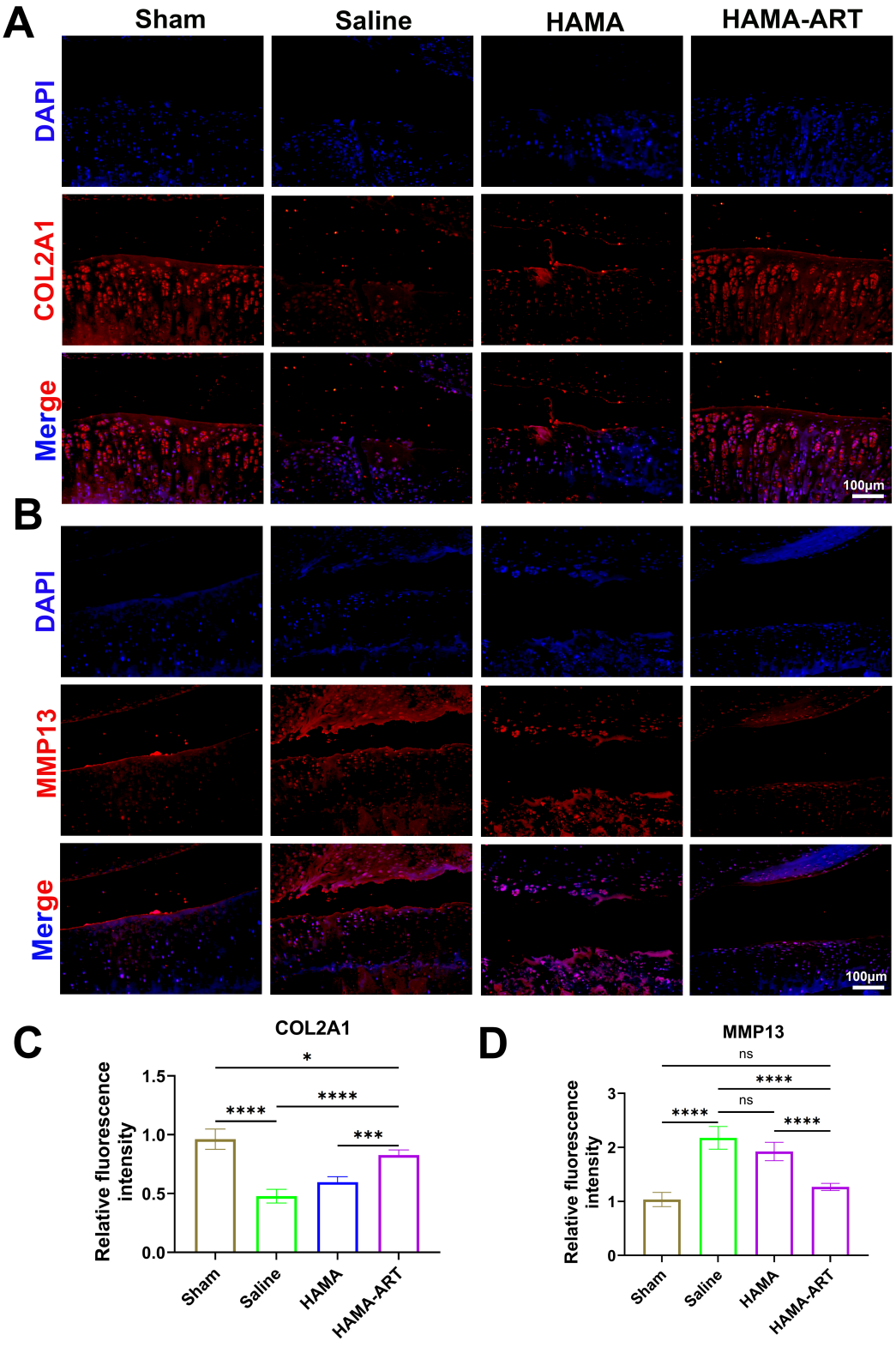


Fig. 8. *In vivo* modulation of cartilage matrix metabolism by HAMA-ART. (**A,B**) Representative *in situ* immunofluorescence images of the anabolic marker *COL2A1* and catabolic enzyme *MMP13* in articular cartilage 8 weeks post-implantation. (**C,D**) Quantification of *COL2A1* and *MMP13* relative fluorescence intensities within the cartilage layer (n = 5) (*$p < 0.05$, ***$p < 0.001$, ****$p < 0.0001$. ns, no significant difference). Fluorescence intensity was quantified using ImageJ, quantitative graphs were generated using GraphPad Prism 10.0, and the figure was assembled using Adobe Photoshop 2021 (Adobe Inc., San Jose, CA, USA).

tural deterioration and cartilage degeneration. These findings suggest that HAMA-ART may provide a localized biomaterial-based strategy for modulating the OA subchondral bone microenvironment.

Pathological SCB remodeling is increasingly recognized as an important contributor to KOA progression rather than merely a secondary consequence of cartilage degeneration [23,26]. This process is closely associated with abnormal osteoblast phenotypes. *Runx2*, a key transcription factor involved in osteogenic differentiation, can be aberrantly upregulated under OA conditions and may contribute to disturbed bone metabolic homeostasis and subchondral bone remodeling [27]. In addition, OA-associated osteoblasts may affect overlying chondrocytes through soluble mediators and osteochondral interface communication, thereby contributing to cartilage matrix imbalance and hypertrophic changes [28,29].

Consistent with this concept, our conditioned medium-transfer experiments showed that soluble factors derived from OA osteoblasts increased *COLX* and *MMP13* expression and reduced *COL2A1* expression in chondrocytes. These findings provide proof-of-concept evidence that OA subchondral osteoblasts can adversely affect chondrocyte matrix metabolism through paracrine mechanisms [30,31]. However, this two-dimensional CM-based model mainly reflects soluble mediator-dependent communication and does not fully reproduce the complex osteochondral interface *in vivo*, including direct cell–cell interactions, extracellular matrix-mediated signaling, mechanical coupling, or spatial diffusion gradients.

In the present study, HAMA-ART treatment attenuated aberrant *Runx2* upregulation in OA osteoblasts, which was accompanied by reduced catabolic and hypertrophic responses in chondrocytes exposed to conditioned medium from treated osteoblasts. Considering the established role of *Runx2* in OA-associated joint degeneration and osteoblast differentiation [32,33], these findings suggest that HAMA-ART-mediated modulation of the OA osteoblast phenotype may contribute to the attenuation of pathological osteoblast–chondrocyte paracrine effects. However, the specific osteoblast-derived mediators responsible for this *Runx*2-associated paracrine communication were not identified in the present study, and the underlying pathway therefore remains to be molecularly characterized. In addition, *Runx2* was assessed only at the protein level; therefore, the current data cannot distinguish whether the observed reduction in *Runx2* resulted from transcriptional suppression, altered protein stability, or other post-translational regulatory mechanisms. Further studies are needed to clarify both the regulation of *Runx2* by ART and the downstream mediators involved in osteoblast–chondrocyte communication.

In addition to its biological effect, the HAMA matrix provided a localized carrier for ART delivery within the SCB defect [34,35]. SEM analysis showed that HAMA-ART retained a porous hydrogel network after ART incorporation, while the total porosity was not significantly changed compared with pure HAMA. Such a porous structure may facilitate fluid exchange and local tissue integration after implantation [36,37]. FTIR analysis further suggested that ART was mainly incorporated into the HAMA network through physical encapsulation rather than new covalent bond formation.

The *in vitro* release assay showed that ART was gradually released from the HAMA-ART hydrogel, supporting its role as a local drug reservoir. Hydrogel networks can regulate molecular diffusion and thereby support sustained local drug release [38]. This sustained release behavior may help prolong local ART exposure within the subchondral defect compared with free-drug administration, which is commonly limited by rapid clearance in the joint environment [24,39]. In addition, the degradation assay showed progressive mass loss of both HAMA and HAMA-ART hydrogels under hyaluronidase-containing conditions, indicating that the HA-based hydrogel matrix was degradable over time [40].

Mechanical characterization is important for hydrogel-based biomaterials because their viscoelastic and compressive properties influence deformation behavior and suitability for tissue-defect filling [41,42]. In this study, ART incorporation did not significantly alter the storage modulus or loss modulus of the HAMA hydrogel, suggesting that the basic viscoelastic properties of the hydrogel were maintained. However, compressive testing showed a lower compressive strength but a higher compressive modulus in HAMA-ART compared with HAMA, indicating increased initial compressive stiffness but reduced ultimate compressive resistance. Therefore, HAMA-ART should be regarded as a localized drug-delivery and defect-filling hydrogel rather than an independent load-bearing substitute for SCB.

Despite these findings, this study has several limitations. First, the therapeutic effect of HAMA-ART was evaluated at a single endpoint of 8 weeks post-implantation, and further studies with multiple time points are needed to clarify the dynamic changes in hydrogel degradation, ART release, SCB remodeling, and cartilage protection *in vivo*. Second, a free ART control group was not included in the animal experiment. Although our strategy mainly focused on localized ART retention within the subchondral bone defect, free ART may be limited by insufficient local retention and rapid clearance in the joint environment [43,44]. Therefore, future studies should further compare free ART administration with HAMA-ART implantation. Third, the conditioned medium-based model used in this study mainly reflects soluble factor-mediated paracrine effects and cannot fully reproduce the complex osteochondral interface *in vivo*. Future studies using larger animal models and three-dimensional osteochondral models will be needed to further validate the therapeutic potential and translational applicability of HAMA-ART [45].

Conclusions

In summary, this study developed an *in situ* photocrosslinkable HAMA-ART hydrogel for localized delivery to the SCB. HAMA-ART attenuated aberrant *Runx2* upregulation in OA osteoblasts and was associated with reduced pathological bone–cartilage crosstalk, ameliorated SCB deterioration, and delayed articular cartilage degradation.

List of Abbreviations

ART, Artemisinin; ALP, Alkaline phosphatase; ARS, Alizarin red S; CCK-8, Cell Counting Kit-8; *COLX*, Type X Collagen; *COL2A1*, Type II Collagen Alpha 1; DMOADs, Disease-Modifying Osteoarthritis Drugs; DMM, Destabilization of the Medial Meniscus; FTIR, Fourier Transform Infrared Spectroscopy; HA, Hyaluronic Acid; HAMA, Hyaluronic Acid Methacrylate; *MMP13*, Matrix Metalloproteinase 13; KOA, Knee Osteoarthritis; *Runx2*, Runt-related transcription factor 2; SCB, Subchondral Bone; SEM, Scanning Electron Microscopy; OA, osteoarthritis; FBS, fetal bovine serum; CM, conditioned medium; WB, western blotting; IF, immunofluorescence; DMSO, dimethyl sulfoxide; UV, ultraviolet; HPLC, high-performance liquid chromatography; OD, optical density; RT, room temperature; BSA, bovine serum albumin; PBST, PBS with Tween-20; TBST, Tris-buffered saline with Tween-20; ECL, enhanced chemiluminescence; SD, Sprague-Dawley; H&E, hematoxylin-eosin; ANOVA, analysis of variance; NSAIDs, nonsteroidal anti-inflammatory drugs; BV/TV, bone volume fraction; Tb.Th, trabecular thickness; Tb.Sp, trabecular separation; PBS, phosphate-buffered saline; RIPA, radioimmunoprecipitation assay lysis buffer; PFA, paraformaldehyde.

Availability of Data and Materials

All data supporting the findings of this study are included within the article and its Supplementary Information. Further inquiries can be directed to the corresponding authors upon reasonable request.

Author Contributions

JXT, CMW and WST contributed to the design of this work. JXT, DZY and SZ contributed to the interpretation of data. MLX, LZ, JZP and TQZ analyzed the data. JXT, DZY, CMW and WT drafted the work. CY, LY and XBT revised critically for important intellectual content. All authors critically reviewed the manuscript for important intellectual content. All authors read and approved the final manuscript. All authors agreed to be accountable for all aspects of the work in ensuring that questions related to the accuracy or integrity of any part of the work were appropriately investigated and resolved.

Ethics Approval and Consent to Participate

This study was approved by the Human Research Ethics Committee of the Affiliated Hospital of Guizhou Medical University (Approval No. 2025-272), and the animal experiment of this study was approved by the Ethics Committee of Laboratory Animals of Guizhou Medical University, approval number: 2502972.

Acknowledgments

We would like to thank Dr. Qiang Zou for his kind help during the research process.

Funding

This work was supported by the National Natural Science Foundation of China [No. 82260428], Guizhou Province High-level Innovative Talents Project [gzwjrs 2023-020], Excellent Reserve Talents Fund of Affiliated Hospital of Guizhou Medical University [gyfyxkrc-2023-11], Provincial Science and Technology Plan Project of Guizhou Province [Grant no. Qiankehe Foundation-ZK [2022] General 453] and Affiliated Hospital of Guizhou Medical University (gyfynsfc[2023]-63).

Conflict of Interest

The authors declare no conflict of interest.

Supplementary Material

Supplementary material associated with this article can be found, in the online version, at https://doi.org/10.22203/eCM.v059a20.

References

[1] Abramoff B, Caldera FE. Osteoarthritis: Pathology, diagnosis, and treatment options. The Medical clinics of North America. 2020; 104: 293–311. https://doi.org/10.1016/j.mcna.2019.10.007.

[2] Loeser RF, Goldring SR, Scanzello CR, Goldring MB. Osteoarthritis: A disease of the joint as an organ. Arthritis & Rheumatism. 2012; 64: 1697–1707. https://doi.org/10.1002/art.34453.

[3] Yao Q, Wu X, Tao C, Gong W, Chen M, Qu M, *et al*. Osteoarthritis: Pathogenic signaling pathways and therapeutic targets. Signal Transduction and Targeted Therapy. 2023; 8: 56. https://doi.org/10.1038/s41392-023-01330-w.

[4] Lajeunesse D, Massicotte F, Pelletier JP, Martel-Pelletier J. Subchondral bone sclerosis in osteoarthritis: Not just an innocent bystander. Modern Rheumatology. 2003; 13: 7–14. https://doi.org/10.3109/s101650300001.

[5] Hu Y, Chen X, Wang S, Jing Y, Su J. Subchondral bone microenvironment in osteoarthritis and pain. Bone Research. 2021; 9: 20. https://doi.org/10.1038/s41413-021-00147-z.

[6] Goldring SR, Goldring MB. Changes in the osteochondral unit during osteoarthritis: Structure, function and cartilage-bone crosstalk. Nature Reviews Rheumatology. 2016; 12: 632–644. https://doi.org/10.1038/nrrheum.2016.148.

[7] Dang Y, Liu Y, Zhang B, Zhang X. Aging microenvironment in osteoarthritis focusing on early-stage alterations and targeted therapies. Bone Research. 2025; 13: 84. https://doi.org/10.1038/s41413-025-00465-6.

[8] Katz JN, Arant KR, Loeser RF. Diagnosis and treatment of hip and

knee osteoarthritis: A review. JAMA. 2021; 325: 568–578. https://doi.org/10.1001/jama.2020.22171.
[9] Latourte A, Kloppenburg M, Richette P. Emerging pharmaceutical therapies for osteoarthritis. Nature Reviews Rheumatology. 2020; 16: 673–688. https://doi.org/10.1038/s41584-020-00518-6.
[10] Evans CH, Kraus VB, Setton LA. Progress in intra-articular therapy. Nature Reviews Rheumatology. 2014; 10: 11–22. https://doi.org/10.1038/nrrheum.2013.159.
[11] Maudens P, Jordan O, Allémann E. Recent advances in intra-articular drug delivery systems for osteoarthritis therapy. Drug Discovery Today. 2018; 23: 1761–1775. https://doi.org/10.1016/j.drudis.2018.05.023.
[12] Pan J, Zhou X, Li W, Novotny JE, Doty SB, Wang L. In situ measurement of transport between subchondral bone and articular cartilage. Journal of orthopaedic research: official publication of the Orthopaedic Research Society. 2009; 27: 1347–1352. https://doi.org/10.1002/jor.20883.
[13] Correa S, Grosskopf AK, Lopez Hernandez H, Chan D, Yu AC, Stapleton LM, *et al*. Translational applications of hydrogels. Chemical Reviews. 2021; 121: 11385–11457. https://doi.org/10.1021/acs.chemrev.0c01177.
[14] Castañeda S, Roman-Blas JA, Largo R, Herrero-Beaumont G. Subchondral bone as a key target for osteoarthritis treatment. Biochemical Pharmacology. 2012; 83: 315–323. https://doi.org/10.1016/j.bcp.2011.09.018.
[15] Burdick JA, Prestwich GD. Hyaluronic acid hydrogels for biomedical applications. Advanced Materials. 2011; 23: H41–H56. https://doi.org/10.1002/adma.201003963.
[16] Liu M, Zeng X, Ma C, Yi H, Ali Z, Mou X, *et al*. Injectable hydrogels for cartilage and bone tissue engineering. Bone Research. 2017; 5: 17014. https://doi.org/10.1038/boneres.2017.14.
[17] Kalairaj MS, Pradhan R, Saleem W, Smith MM, Gaharwar AK. Intra-articular injectable biomaterials for cartilage repair and regeneration. Advanced Healthcare Materials. 2024; 13: e2303794. https://doi.org/10.1002/adhm.202303794.
[18] Gan D, Tao C, Jin X, Wu X, Yan Q, Zhong Y, *et al*. Piezo1 activation accelerates osteoarthritis progression and the targeted therapy effect of artemisinin. Journal of Advanced Research. 2024; 62: 105–117. https://doi.org/10.1016/j.jare.2023.09.040.
[19] Zheng X, Yu B, Song Y, Chen Y, Li Z, Yao J. Artemisinin exerts anti-inflammatory effects in osteoarthritis through the inhibition of TGF-β1 signaling. Frontiers in Immunology. 2026; 17: 1717045. https://doi.org/10.3389/fimmu.2026.1717045.
[20] Sanchez C, Deberg MA, Piccardi N, Msika P, Reginster JY, Henrotin YE. Subchondral bone osteoblasts induce phenotypic changes in human osteoarthritic chondrocytes. Osteoarthritis and Cartilage. 2005; 13: 988–997. https://doi.org/10.1016/j.joca.2005.07.012.
[21] Gong X, Xie W, Wang B, Gu L, Wang F, Ren X, *et al*. Altered spontaneous calcium signaling of in situ chondrocytes in human osteoarthritic cartilage. Scientific Reports. 2017; 7: 17093. https://doi.org/10.1038/s41598-017-17172-w.
[22] Höger SA, Cong T, Hall AJ, Lane J, Runer A. Subchondral bone contribution to osteochondral health and injury. Annals of Joint. 2025; 10: 27. https://doi.org/10.21037/aoj-25-12.
[23] Hu W, Chen Y, Dou C, Dong S. Microenvironment in subchondral bone: Predominant regulator for the treatment of osteoarthritis. Annals of the Rheumatic Diseases. 2021; 80: 413–422. https://doi.org/10.1136/annrheumdis-2020-218089.
[24] Gao J, Xia Z, Mary HB, Joseph J, Luo JN, Joshi N. Overcoming barriers for intra-articular delivery of disease-modifying osteoarthritis drugs. Trends in Pharmacological Sciences. 2022; 43: 171–187. https://doi.org/10.1016/j.tips.2021.12.004.
[25] Gupta A, Lee J, Ghosh T, Nguyen VQ, Dey A, Yoon B, *et al*. Polymeric hydrogels for controlled drug delivery to treat arthritis. Pharmaceutics. 2022; 14: 540. https://doi.org/10.3390/pharmaceutics14030540.
[26] Burr DB, Gallant MA. Bone remodelling in osteoarthritis. Nature Reviews Rheumatology. 2012; 8: 665–673. https://doi.org/10.1038/nrrheum.2012.130.
[27] Chen D, Kim DJ, Shen J, Zou Z, O'Keefe RJ. Runx2 plays a central role in osteoarthritis development. Journal of Orthopaedic Translation. 2019; 23: 132–139. https://doi.org/10.1016/j.jot.2019.11.008.
[28] Yuan XL, Meng HY, Wang YC, Peng J, Guo QY, Wang AY, *et al*. Bone-cartilage interface crosstalk in osteoarthritis: Potential pathways and future therapeutic strategies. Osteoarthritis and Cartilage. 2014; 22: 1077–1089. https://doi.org/10.1016/j.joca.2014.05.023.
[29] Lories RJ, Luyten FP. The bone–cartilage unit in osteoarthritis. Nature Reviews Rheumatology. 2011; 7: 43–49. https://doi.org/10.1038/nrrheum.2010.197.
[30] Zhang S, Li T, Feng Y, Zhang K, Zou J, Weng X, *et al*. Exercise improves subchondral bone microenvironment through regulating bone-cartilage crosstalk. Frontiers in endocrinology. 2023; 14: 1159393. https://doi.org/10.3389/fendo.2023.1159393.
[31] Kaya S, Bailey KN, Schurman CA, Evans DS, Alliston T. Bone-cartilage crosstalk informed by aging mouse bone transcriptomics and human osteoarthritis genome-wide association studies. Bone Reports. 2022; 18: 101647. https://doi.org/10.1016/j.bonr.2022.101647.
[32] Kamekura S, Kawasaki Y, Hoshi K, Shimoaka T, Chikuda H, Maruyama Z, *et al*. Contribution of runt-related transcription factor 2 to the pathogenesis of osteoarthritis in mice after induction of knee joint instability. Arthritis & Rheumatism. 2006; 54: 2462–2470. https://doi.org/10.1002/art.22041.
[33] Komori T. Regulation of proliferation, differentiation and functions of osteoblasts by Runx2. International journal of molecular sciences. 2019; 20: 1694. https://doi.org/10.3390/ijms20071694.
[34] Li J, Mooney DJ. Designing hydrogels for controlled drug delivery. Nature Reviews Materials. 2016; 1: 16071. https://doi.org/10.1038/natrevmats.2016.71.
[35] Chen J, Deng M, Wang J, Liu Y, Hu Z, Luan F, *et al*. Recent advances in injectable hydrogels for osteoarthritis treatments. Frontiers in Bioengineering and Biotechnology. 2025; 13: 1644222. https://doi.org/10.3389/fbioe.2025.1644222.
[36] Annabi N, Nichol JW, Zhong X, Ji C, Koshy S, Khademhosseini A, *et al*. Controlling the porosity and microarchitecture of hydrogels for tissue engineering. Tissue Engineering Part B: Reviews. 2010; 16: 371–383. https://doi.org/10.1089/ten.teb.2009.0639.
[37] Grodzicka M, Gąsior G, Jędrzejewski T, Wrotek S, Madajski P, Radtke A. Porous iron scaffolds with the addition of manganese and copper: Physicochemical characteristics and biocompatibility analysis. European Cells & Materials. 2025; 54: 128–144. https://doi.org/10.22203/eCM.v054a09.
[38] Lin CC, Metters AT. Hydrogels in controlled release formulations: Network design and mathematical modeling. Advanced Drug Delivery Reviews. 2006; 58: 1379–1408. https://doi.org/10.1016/j.addr.2006.09.004.
[39] Jones IA, Togashi R, Wilson ML, Heckmann N, Vangsness CT Jr. Intra-articular treatment options for knee osteoarthritis. Nature Reviews Rheumatology. 2019; 15: 77–90. https://doi.org/10.1038/s41584-018-0123-4.
[40] Highley CB, Prestwich GD, Burdick JA. Recent advances in hyaluronic acid hydrogels for biomedical applications. Current Opinion in Biotechnology. 2016; 40: 35–40. https://doi.org/10.1016/j.copbio.2016.02.008.
[41] Stammen JA, Williams S, Ku DN, Guldberg RE. Mechanical properties of a novel PVA hydrogel in shear and unconfined compression. Biomaterials. 2001; 22: 799–806. https://doi.org/10.1016/S0142-9612(00)00242-8.
[42] Drury JL, Mooney DJ. Hydrogels for tissue engineering: Scaffold design variables and applications. Biomaterials. 2003; 24: 4337–4351. https://doi.org/10.1016/S0142-9612(03)00340-5.
[43] Gerwin N, Hops C, Lucke A. Intraarticular drug delivery in os-

teoarthritis. Advanced Drug Delivery Reviews. 2006; 58: 226–242. https://doi.org/10.1016/j.addr.2006.01.018.

[44] Rai MF, Pham CT. Intra-articular drug delivery systems for joint diseases. Current Opinion in Pharmacology. 2018; 40: 67–73. https://doi.org/10.1016/j.coph.2018.03.013.

[45] Malfait AM, Little CB. On the predictive utility of animal models of osteoarthritis. Arthritis Research & Therapy. 2015; 17: 225. https://doi.org/10.1186/s13075-015-0747-6.

Editor's note: The Scientific Editors responsible for this paper were Xiaolei Zhang and Martin Stoddart.

Received: 25th April 2026; **Accepted**: 5th September 2026; **Published**: 30th October 2026